Post-Print

This is the accepted version of:

A. Pasquale, S. Silvestrini, A. Capannolo, P. Lunghi, M. Lavagna
Small Bodies Non-Uniform Gravity Field On-Board Learning Through Hopfield Neural Networks
Planetary and Space Science, Vol. 212, 2022, 105425 (14 pages)
doi:10.1016/j.pss.2022.105425

Small Bodies Non-Uniform Gravity Field On-Board Learning Through Hopfield Neural Networks

Andrea Pasquale[a,1,*], Stefano Silvestrini[a,2], Andrea Capannolo[a,3], Paolo Lunghi[a,4], Michèle Lavagna[a,5]

[a]*Politecnico di Milano, Via La Masa 34, 20156, Milano*

Abstract

Small bodies environment is usually difficult to be modelled for a number of reasons. Among the others, the uncertainty associated to the non-uniform gravitational field requires in-situ observations for its refinement, or its identification. This operation becomes even more challenging in case the orbiting platform is a CubeSat or, in general, a platform with reduced computational power as well as a high autonomy requirement. In this paper, a new approach to reconstruct on-board the gravity field of either unknown or partially known bodies is presented. In particular, the use of a Hopfield Neural Network (HNN) to reconstruct the coefficients of a Spherical Harmonics Expansion (SHE), that is assumed to approximate the gravity field of the body, is described. A comparison with an Extended Kalman Filter (EKF) used for parameter estimation is presented and the differences of the two methods are critically discussed: due to the structure of the HNN, the former results to be computationally faster and lighter than a stand-alone EKF used for parameter estimation.

Keywords: Hopfield Neural Network (HNN), asteroid proximity operations, gravity field identification, online learning, parameter estimation

1. Introduction

Asteroid and comets have become of great importance during the last decade, due to the enormous scientific return they can provide to understand the origins of our Solar System. Their exploration, however, poses enormous challenges from an engineering point of view. Generally, poor knowledge of physical properties of these objects, such as mass and density, and of their shape, translates into a rough estimation of the gravitational environment. In missions design, risks coming from this lack of knowledge are generally mitigated by a safe trajectory design, limiting the spacecraft proximity to the targeted body, at the cost of lower quality in observations and measurements. To reduce distance, rapidity in the operations becomes of the utmost importance, and only autonomous systems for the guidance, navigation and control of the spacecraft can be adopted. To do so, the spacecraft must be able to reconstruct the dynamical environment and counteract the gravitational perturbations coming from the uneven shape of the asteroid and other sources, such as the solar radiation pressure. At the current time, there have been a certain number of missions that use radio-science to estimate the higher-order terms of the gravitational potential of those kind of objects [1, 2, 3]. This technique, however, works well for large bodies but its accuracy decreases drastically for smaller bodies due to the uncertainties arising from the Solar Radiation Pressure (SRP).

Past studies dealt with the problem of reconstructing the unknown acceleration terms of the dynamics, for example exploiting an augmented Kalman filter for the estimation of

*Corresponding author
[1]PhD Candidate, DAER, Politecnico di Milano - andrea.pasquale@polimi.it
[2]Postdoctoral Researcher, DAER, Politecnico di Milano - stefano.silvestrini@polimi.it
[3]PhD Candidate, DAER, Politecnico di Milano - andrea.capannolo@polimi.it
[4]Assistant Professor, DAER, Politecnico di Milano - paolo.lunghi@polimi.it
[5]Full Professor, DAER, Politecnico di Milano - michelle.lavagna@polimi.it

such unmodelled inputs [4, 5, 6]. While this approach can be advantageous from a pure guidance and navigation perspective, it lacks insight for what concerns the direct knowledge of the target's shape and gravitational properties, being them blended to the other perturbative effects in the overall disturbance acceleration. In such sense, it is desirable to exploit a technique dedicated to the reconstruction of the small body's shape and gravity field, to aid the navigation of the spacecraft, while enriching the science output of the mission. There have been a number of studies that propose different applications of machine learning to this problem: in [7] a single layer forward network, designed and trained by means of Extreme Learning Machines, is shown to be capable to learn the relationship between the spacecraft position and the gravitational acceleration. In [8], neural reinforcement learning is used to control a spacecraft around a celestial body whose gravity field is unknown. In [9], finally, an efficient gravity field modeling method based on Gaussian process regression is presented, that uses a kind of (supervised) Bayesian regression to reconstruct the relationship between the gravitational acceleration and check point. However, those methods have to be trained before use. This is possible if the target body shape is already available and so need a detailed a-priori knowledge of the target body is available.

Other examples can be the use of Back Propagation Artificial Neural Networks (BPANN) for the Earth gravity field approximation is presented in [10] and the use of Artificial Neural Networks (ANN) in [11] for a body gravity field interpretation. It is of interest from this point of view, the use of Radial Basis Function (RBF)-based networks that are an alternative to the popular Multi-Layer Perceptron (MLP) (e.g. the Single Layer Forward Network (SLFN) and the ANN discussed before) [12]. Moreover, in [13] and [12] it has been shown that a RBF-based networks can be used for the *online* identification of non-linear system.

More recently, in [14] the use of a neural network based on a Modified State Observer (MSO) is presented. It uses the MSO for estimating the uncertainties that a satellite may experience while in orbit, with the primary advantage that the neural network is trained *online*. This method appears to be one among the most promising but it reconstructs the gravity field in a indirect way: in fact, the accelerations time history along three axis as (a_x, a_y, a_z) is reconstructed, without giving any other information. A forward least-square optimization method must be then used in order to have a global, time independent representation of the gravity field in the form of a spherical harmonics expansion.

In this paper we explore the possibility to use a specifically tailored Hopfield Neural Network (HNN) to overcome this problem and to estimate the attractor's gravity field directly online, with no a-priori knowledge of the attractor and recovering a global representation of the field. Through a numerical simulation campaign, HNN is demonstrated to be a valid solution to the problem, due to its flexibility, adaptation to new inputs and the reduced computational burden. The HNN results then the perfect candidate for fast autonomous correction in the implemented dynamics and target reconstruction. In brief, the contributions of the paper are:

- to propose an HNN to be used to reconstruct the global gravitational field of unknown or poorly known bodies;
- to highlight the dependence of the HNN hyper-parameters to the physical properties of the target body as well as to the orbit used for the identification;
- to extend the gravitational field identification problem to multi-body dynamical

environments (binary systems in this case);

- to compare performances and computational cost of a EKF-HNN combination, for state & parameter identification respectively, with a EKF used for both tasks together.

The paper is organized as follows. Section 2 is dedicated to he review of the dynamics background, as well as the theory behind the neural network. Section 3 describes the procedure to reconstruct the gravity field through the adopted network. Section 5 introduces and tests a Kalman filter with extended state for the estimation of coefficients, and compares its results to the proposed network approach, in terms of performance and computational time. Finally, conclusions on the proposed method are discussed in Section 6.

2. Background & Tools

Some assumptions are made both on the dynamical environment as well as the output of the reconstruction in order to solve the problem of the reconstruction of the gravitational field of an unknown, arbitrary shaped body directly on-board of a spacecraft orbiting it.

2.1. Dynamical Environment

The orbital environments about small bodies are among the highly perturbed environments found in the solar system [15]. In this work two simplified environmental models are considered: the one associated with a single body, based on the so called Perturbed Two-Body Problem (P2BP), and the one associated to a binary system of bodies, based

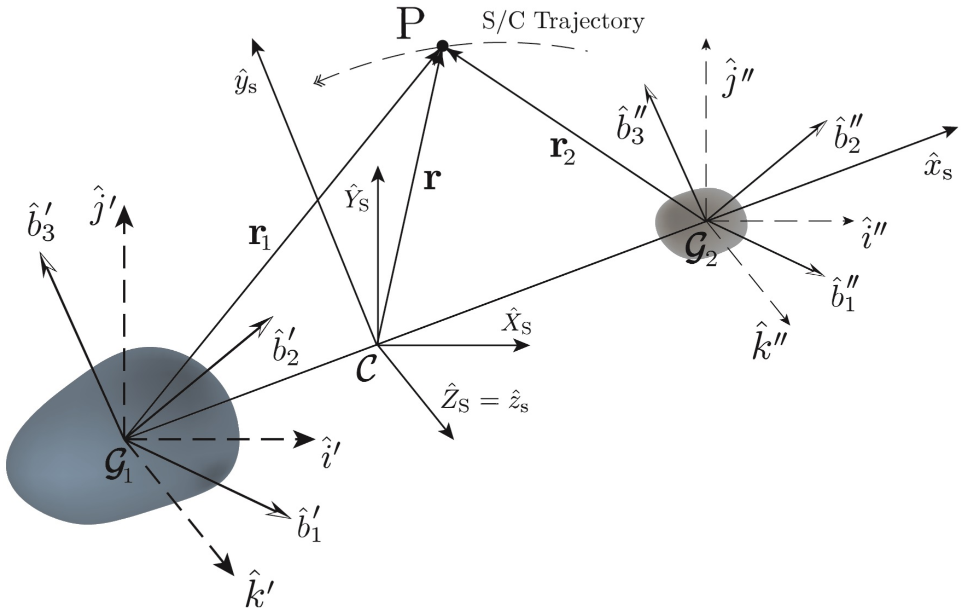

Figure 1: Geometry of the MCR3BP

on the Modified Circular Restricted Three-Body Problem (MCR3BP). This, in order to test the scalability of the network to different dynamical environments, both from the formulation as well as from the identification performance point of view. These models are extensively discussed in [16],[17].

2.1.1. *The P2BP*

The detailed derivation of the dynamical environment model associated to a single body relies on the P2BP model. Here the equations of motion for a reduced order model are briefly recalled. Under the assumption that the body rotates about its principal inertia axis with uniform angular velocity Ω, the equations of motion written in the body-fixed frame are:

$$\begin{cases} \ddot{x} - 2\Omega\dot{y} = \Omega^2 x + a_{T,x} \\ \ddot{y} + 2\Omega\dot{x} = \Omega^2 y + a_{T,y} \\ \ddot{z} = a_{T,z} \end{cases} \tag{1}$$

wherein the acceleration model adopted can be expressed as:

$$\mathbf{a}_{\mathrm{T}}(\mathbf{r}, \mathbf{s}, \mathbf{d}_{\mathrm{k-a}}) = \mathbf{a}_{\mathrm{G}}(\mathbf{r}) + \mathbf{a}_{\mathrm{SRP}}(\mathbf{r}, \mathbf{s}) + \sum_{k=1}^{N} \mathbf{a}_{\mathrm{3rd_k}}(\mathbf{r}, \mathbf{d}_{\mathrm{k-a}}) \tag{2}$$

being $\mathbf{a}_{\mathrm{G}}$ the gravitational acceleration due to the gravity field of the body, $\mathbf{a}_{\mathrm{SRP}}$ the acceleration contribution due to the SRP and $\mathbf{a}_{\mathrm{3rd_k}}$ the acceleration contribution due to the k-th third-body. In this work, since the aim is to focus the attention on the gravity field reconstruction, the other perturbations are neglected and the gravitational model used as ground truth is the constant density polyhedron [18]. Then, the model is a subclass of the P2BP, called in this work Shape-Based Two-Body Problem (S2BP).

2.1.2. The MCR3BP

The geometry and the formulation of the MCR3BP starts from the one of the Circular Restricted Three-Body Problem (CR3BP). The only difference is that the two bodies are assumed to have a certain shape and not to be point masses. In particular, the MCR3BP may be formulated as follows.

First of all, the angular velocity associated to the two-body motion of the primaries is computed:

$$\Omega_S = \sqrt{\frac{G(m_1 + m_2)}{d_{12}^2}} \tag{3}$$

with m_1 and m_2 are the mass of the primary and the secondary, d_{12} the distance between them and G the gravitational constant. Then, with reference to Fig. 1, the following reference frames are defined:

- $\mathcal{T}_S = (\mathcal{C};\, \hat{X}_s, \hat{Y}_s, \hat{Z}_s)$, a quasi-inertial frame, fixed at the center of mass of the two primaries;
- $\mathcal{T}_s = (\mathcal{C};\, \hat{x}_s, \hat{y}_s, \hat{z}_s)$, a synodic frame, fixed at the center of mass of the two primaries and rotating with Ω_S which respect to $\mathcal{T}_S$;
- $\mathcal{T}_n^k = (\mathcal{G}_k;\, \hat{\imath}^k, \hat{\jmath}^k, \hat{k}^k)$, a quasi-inertial frame, centred in the k-th body and parallel to $\mathcal{T}_S$;
- $\mathcal{T}_b^k = (\mathcal{G}_k;\, \hat{b}_1^k, \hat{b}_2^k, \hat{b}_3^k)$, a body frame, centred in the k-th body and rotating with Ω_k with respect to $\mathcal{T}_n^k$;

Then the spacecraft position vector $\mathbf{r}$, in the $\mathcal{T}_s$ frame can be expressed in the k-th body fixed frame, $\mathcal{T}_b^k$ according to:

$$\mathbf{r}^{(k)} = \mathrm{T}_n^k \cdot \mathrm{T}_{\Omega_S}^T (\mathbf{r} - \mathbf{l}_k) \tag{4}$$

where here $\mathbf{l}_k$ is the distance of the primary to the centre of mass of the system in the $\mathcal{T}_s$ reference. Note that the product $\mathrm{T}_n^k \cdot \mathrm{T}_{\Omega_S}^T$ can be re-arranged, having defined the differential rotation as $\Delta\Omega_k = \Omega_S - \Omega_k$, since:

$$\mathrm{T}_{\Omega_S} \cdot \mathrm{T}_n^{k\,T} = \begin{bmatrix} \cos(\Delta\Omega_k t) & \sin(\Delta\Omega_k t) & 0 \\ -\sin(\Delta\Omega_k t) & \cos(\Delta\Omega_k t) & 0 \\ 0 & 0 & 1 \end{bmatrix} = \mathrm{T}_\Delta^k(t) \tag{5}$$

The equation of motion in the $\mathcal{T}_s$ frame results, according to [16]:

$$\ddot{\mathbf{r}} + \boldsymbol{\Omega}_S \times (\boldsymbol{\Omega}_S \times \mathbf{r}) + 2\boldsymbol{\Omega}_S \times \mathbf{r} = \mathrm{T}_\Delta^1(t)\nabla\mathcal{U}_1\left(\mathbf{r}^{(1)}\right) + \mathrm{T}_\Delta^2(t)\nabla\mathcal{U}_2\left(\mathbf{r}^{(2)}\right) \tag{6}$$

Here $\mathcal{U}_1$ is the gravitational potential of the primary and $\mathcal{U}_2$ the one of the secondary. This work implement a simpler version of Eq. 6. In particular, the bodies are assumed to be locked with the respect to the synodic frame resulting in a Shape-Based CR3BP (SCR3BP):

$$\ddot{\mathbf{r}} + \boldsymbol{\Omega}_S \times (\boldsymbol{\Omega}_S \times \mathbf{r}) + 2\boldsymbol{\Omega}_S \times \mathbf{r} = \nabla\mathcal{U}_1(\mathbf{r}_1) + \nabla\mathcal{U}_2(\mathbf{r}_2) \tag{7}$$

where here $\mathcal{U}_i(\cdot)$ is the gravitational potential associated to the i-th body.

2.2. The Parametric Identification Problem

As a global approximation technique of the true gravitational field, the Spherical Harmonics Expansion (SHE) has been largely studied and applied for mission analysis purposes in the past years [19],[20],[21]. Being an analytical model, it results to be computationally efficient and light to be evaluated, if compared with constant density polyhedron or mascons models, which makes it suitable for various applications. In a SHE, the gravity field of the body is assumed to be represented through a potential of the form:

$$\mathcal{U} = \frac{\mu}{r} - \frac{\mu}{r}\sum_{n=2}^{N}\left(\frac{R_0}{r}\right)^n\left[J_n\mathcal{P}_n^0(\cos\theta) - \sum_{m=1}^{n}(C_{nm}\cos(m\lambda) + S_{nm}\sin(m\lambda))\mathcal{P}_n^m(\cos\theta)\right] \quad (8)$$

Here θ is the colatitude, λ the longitude, r the radial distance to the center of mass of the body, R_0 a reference radius, $\mathcal{P}_n^m(x)$ Associated Legendre Polynomials (ALP) of degree n and order m and μ the body gravitational parameter. For the peculiar properties of the model, the SHE is assumed to be reconstructed in this work. Hence, the objective becomes to estimate the coefficients J_n,C_{nm} and S_{nm} of the expansion, while μ is assumed to be known. In particular, the model to be reconstructed, in the case of the S2BP, is the following:

$$\ddot{\mathbf{r}} + \boldsymbol{\Omega} \times (\boldsymbol{\Omega} \times \mathbf{r}) + 2\boldsymbol{\Omega} \times \mathbf{r} = \nabla\mathcal{U}(\mathbf{r}) \quad (9)$$

Writing the SHE in a matrix form, then the model can be written as:

$$\ddot{\mathbf{r}} + \boldsymbol{\Omega} \times (\boldsymbol{\Omega} \times \mathbf{r}) + 2\boldsymbol{\Omega} \times \mathbf{r} = -\frac{\mu}{r^3}\mathbf{r} + \mathrm{A}(\mathbf{r}) \cdot \mathbf{C} \quad (10)$$

Where here, the vector $\mathbf{C}$ contains all the coefficients of the expansion to be estimated. Now, defining:

$$\mathbf{y} = \ddot{\mathbf{r}} + 2\boldsymbol{\Omega} \times \dot{\mathbf{r}} + \boldsymbol{\Omega} \times (\boldsymbol{\Omega} \times \mathbf{r}) + \frac{GM}{r^3}\mathbf{r} \quad (11)$$

The model can be written in the so called Linear-in-parameters (LIP) form:

$$\mathbf{y} = \mathrm{A}(\mathbf{r}) \cdot \mathbf{C} \quad (12)$$

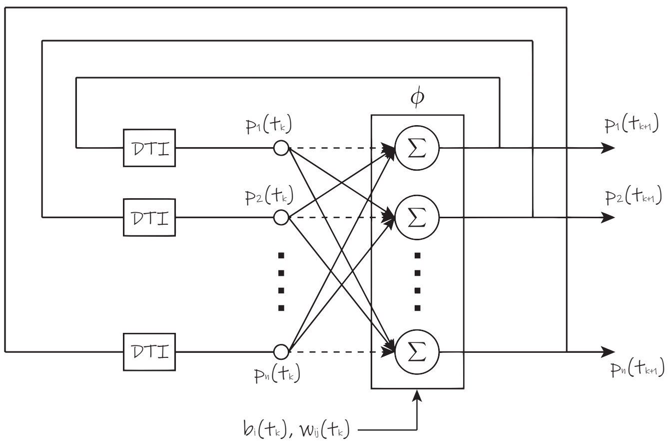

Figure 2: The Hopfield Neural Network structure.

According to [22, 23], being the model linear in the parameters, the identification problem can be reformulated as an optimization problem. In particular, defining the *prediction error* $\mathbf{e} = \mathbf{y} - \mathrm{A} \cdot \mathbf{C}^*$, where $\mathbf{C}^*$ is the estimation of $\mathbf{C}$, the resulting combinatorial optimization problem is [17]:

$$\min_{\mathbf{C}} \left\{ \sup_{t} \left(\frac{1}{2} \mathbf{e}^T \cdot \mathbf{e} \right) \right\} \tag{13}$$

With a similar procedure, the formulation can be extended to the MCR3BP.

2.3. Hopfield Neural Networks

HNNs are a kind of ANNs formulated by Hopfield in its paper [24]. The model as well as its stability has been extensively studied in the last decades. In the original Hopfield's formulation of the network, the dynamics of the neuron i is governed by the ODE, [22]:

$$\frac{dp_i}{dt} = -p_i(t) + \sum_{j=1}^{N} w_{ij} \phi_j(p_j(t)) - b_i(t)) \tag{14}$$

where $p_i(t)$ is the total input to the neuron i, ϕ_j is a continuous non-linear, bounded and strictly increasing function called *activation function*, and w_{ij} and b_i are parameters corresponding respectively to the synaptic efficiency associated with the connection from neuron j to neuron i, and the bias of the neuron i. The neuron state is then obtained through the activation function, $\phi(z) = \tanh z$:

$$s_i(t) = \tanh\left(\frac{p_i(t)}{\beta}\right) = \phi(p_i, \beta) \tag{15}$$

where $\beta > 0$ is a coefficient to eventually regulate the slope of the activation function. According to [22, 24], in order to prove that the neural system defined in Eq. 14 is stable, Lyapunov stability theory is exploited. In this paper, Abe [25] modified formulation of the network is used, being the most suited for combinatorial optimization problems. In this case, the Lyapunov function is defined as:

$$V(\mathbf{s}) = -\frac{1}{2}\sum_{i=1}^{n}\sum_{j=1}^{n} w_{ij} s_i s_j + \sum_{i=1}^{n} b_i s_i \tag{16}$$

The key concept associated to the theory of HNN is the fact that:

$$\frac{\partial V}{\partial s_i} = -\frac{dp_i}{dt} \tag{17}$$

so that the network defines a gradient system and thus *the network states evolve in the direction that minimized the Lyapunov function.* So the application of Hopfield networks to the solution of optimization problems is a direct consequence of the dynamical properties of the network and, in particular, of the existence of the Lyapunov function. Then, the HNN is formulated as an ODE, that can be represented as a recurrent dynamics, as in Fig.2:

$$\frac{dp_i}{dt} = \sum_{j=1}^{N} w_{ij}\phi_j(p_j) - b_i = net_i(t) \tag{18}$$

Applying the chain rule, the recurrent neuron dynamics can be reduced to:

$$\frac{d\mathbf{s}}{dt} = \frac{1}{\beta}\mathrm{D}\Big(\mathrm{W}\mathbf{s} + \mathbf{b}\Big) \tag{19}$$

where $\mathbf{s}(t)$ is neuron states vector, β an hyper-parameter of the network, $\mathrm{D} = \mathrm{diag}(1 - s_i^2)$, $\mathrm{W} = -\mathrm{A}^T\mathrm{A}$ is called *weight matrix* and $\mathbf{b} = \mathrm{W}\mathbf{s}_0 + \mathrm{A}^T\mathbf{y}$ is called *bias vector*. Note that both the weight matrix and the bias vector are associated to the SHE model and can be recovered matching the Lyapunov function of the network with the cost function of the optimization problem [26, 23]. Here $\mathbf{s}_0 = \mathbf{s}(0)$. The proof of the stability of the method is presented in [23, 16], thus is not reported here.

2.4. Discrete-time Hopfield Neural Network

Usual discrete versions of HNN include Backward Euler methods. However, according to [27] a better discrete version of the network is:

$$(s_i)_{k+1} = \frac{(s_i)_k + \tanh\left(\frac{h}{\beta}(net_i)_k\right)}{1 + (s_i)_k \tanh\left(\frac{h}{\beta}(net_i)_k\right)} \tag{20}$$

where h is the time-step, $(s_i)_k$ is the state of the i-th neuron at the k-th step and

$$(net_i)_k = \sum_j (w_{ij})_k (s_j)_k - (b_i)_k \tag{21}$$

Note that this version is bounded but is not continuous whenever the denominator is zero. In principle, this condition cannot be achieved since $|s_i| < 1$, but, due to numerical round-off errors, it has to be taken into account in a computer implementation of the discrete method. In this study, the choice is to set $(s_i)_{k+1} = (s_i)_k$ whenever the singularity is encountered. This discrete version of the network, however, still suffers from the time step choice [16].

3. Gravity Field Identification of Small Solar System Objects with HNN

The gravitational field reconstruction of a group of test objects through the use of a HNN is analysed in this section with the aim to highlight dependencies with respect to initial orbital conditions as well as the network tuning parameters. Since the aim is to test the HNN capability of computing correctly the SHE's Stokes coefficients, the following assumptions are considered:

- The minor body is considered to be non rotating;
- A perfect determination is assumed for the state of the orbiting object: the state vector is, in fact, assumed to be known and expressed with respect to the exact centre of mass of the body; this assumed only for this section, where the method is developed and validated from the conceptual point of view.
- Sun third body gravitational perturbation and SRP are neglected.
- The mass of the body is considered to be known. This is a major assumption, since it is a parameter to be estimated too, because the Stokes coefficients and M are strongly correlated. Indeed, a simultaneous estimation of the mass and the coefficients is not possible here, since in that case the LIP form in Eq. 12 cannot be recovered. However, as shown in [16], it is possible to estimate the mass of the body prior to the one of the coefficients. Furthermore, the correlation of the

coefficients on the gravitational parameter $\mu = GM$ can be removed from the estimation introducing a normalization to the equation of motion. In particular, defining a reference two-body acceleration:

$$a_{\text{ref}} = \frac{\mu}{R_{\text{ref}}^2} \tag{22}$$

and considering $\tilde{q}$ the normalized version of a quantity q, Eq. 1 becomes:

$$\begin{cases} \tilde{x}'' - 2\tilde{y}' & = \tilde{x} - \left(\frac{R_{\text{ref}}}{r}\right)^2 \frac{\tilde{x}}{\tilde{r}} + \frac{R_{\text{ref}}^2}{\mu}\frac{\partial \mathcal{U}_p}{\partial x} \\ \tilde{y}'' + 2\tilde{x}' & = \tilde{y} - \left(\frac{R_{\text{ref}}}{r}\right)^2 \frac{\tilde{y}}{\tilde{r}} + \frac{R_{\text{ref}}^2}{\mu}\frac{\partial \mathcal{U}_p}{\partial y} \\ \tilde{z}'' & = - \left(\frac{R_{\text{ref}}}{r}\right)^2 \frac{\tilde{z}}{\tilde{r}} + \frac{R_{\text{ref}}^2}{\mu}\frac{\partial \mathcal{U}_p}{\partial x} \end{cases} \tag{23}$$

This version of Eq. 1 is particularly useful to be used in the neural network since the weight and bias matrix results to be normalized. This process is here presented for the S2BP but can be extended to the SCR3BP. The choice of R_{ref} is also important: to decouple the problem at the most with respect to both the body and the orbit, R_{ref} is taken to be equal to $r(t_k)$, in such a way:

$$\left| \frac{r^2(t)}{\mu} \nabla \mathcal{U}_{n,m}(r) \right| \leq 1$$

where here $\mathcal{U}_{n,m}$ is the n-th degree, m-th order SHE term of the expansion.

As highlighted in the previous section, the HNN and its convergence are fully determined once $\beta, \mathbb{W}, \mathbf{b}$ and $\mathbf{s}_0$ are given. Thus, once the initial conditions on the orbit i.e. $\mathbf{r}(t_0)$ and $\mathbf{v}(t_0)$ are given and the newtork is initialized with a given $\mathbf{s}(t_0)$, then the performances would depends on the value of the hyper-parameter, β. Then, in general, the i-th coefficient converge is a function of:

$$C_i(t_k) = s_i(\text{body}, \mathbf{x}(t_k), \beta, \mathbf{s}(t_k)) \tag{24}$$

i.e. the i-th coefficient is coincident with the neuron state, $s_i(t_k)$, which is determined as $s_i(t_k) = \phi(\mathbf{s}(t_{k-1}), \beta)$ where here $\phi(\cdot)$ is the activation function. In particular, the neurons state dynamics is fully determined by:

- the **body**, in terms of its shape (S) and mass (M);
- the **orbital state**, $\mathbf{x}(t_k)$: note that the dependence on the state can be written in terms of the current osculating elements associated to the trajectory $(a, e, i, \Omega, \omega, \nu)$. Moreover, since $\mathbf{x}(t_k)$ depends on $\mathbf{x}(t_0)$ and t_k, the latter can be considered as independent variables.
- the **network hyper-parameter**, β: with reference to Fig. 15 small values of β are associated with a steeper activation function and so to an activation that is more sensitive to the inputs. On the other hand, values of $\beta \geq 1$ make the activation less sensitive.
- the **network neuron states**, $s_j(t_k)$: since the i-th neuron dynamics is also associated to all the other j-th neurons, as seen in Eq. 18. This means that the neuron state behaviour is associated to the number of coefficients (N_C) that are estimated.

Then, the neuron state can be expressed as:

$$C_i(t_k) = s_i(S, M, a_0, e_0, i_0, \Omega_0, \omega_0, \beta, N_C, t_k, \mathbf{s}_0) \tag{25}$$

Finally, an integral measure of the error of the i-th reconstructed coefficient, $C_i(t)$, with respect to its the real value, $\bar{C}_i$, is then introduced:

$$\mathrm{iMSE}_i = \frac{1}{2N} \sum_{k}^{N} \frac{\sqrt{(C_i(t_k) - \bar{C}_i)^2}}{\bar{C}_i} \tag{26}$$

This parameter of merit is an integral measure that weights both the accuracy and the velocity of the network. In the following analysis the neuron convergence dependency on the different parameters is analysed by means of the **iMSE**. The flowchart that brings from the initial condition to the Stokes coefficients identification is then the following:

1. The initial orbit is propagated for a certain period, T, with a time-step h using the P2BP model;
2. The network is initialized with $\mathbf{s}_0 = \mathbf{0}$;
3. Positions and velocities at each instant t_k are retrieved;
4. $\mathbf{y}_k$ in Eq. 11 is computed, approximating by finite differences the acceleration and assuming the body to uniformly rotating about its principal inertia axis;
5. The weight matrix $\mathbf{W}(t_k)$ and the bias vector $\mathbf{b}(t_k)$ are computed;
6. The neuron state (discrete) dynamics is retrieved by means of Eq. 20, providing the estimates for C_is at each instant.

3.1. Dependency on body mass

The normalization introduced *cancel* the direct dependency on the body mass. Then:

$$C_i(t_k) = s_i(S, \_\_, a_0, e_0, i_0, \Omega_0, \omega_0, \beta, N_C, t_k, \mathbf{s}_0) \tag{27}$$

However the body mass re-enter the problem in the optimal choice of β:

$$\beta^* = \beta^*(M, \dots) \tag{28}$$

Being the dependency on mass and body shape strictly connected, the optimal β is not trivial. However, as shown in the following paragraph, the actual dependence on the body shape is negligible. Therefore, as shown in [16]:

- In general, the optimal β choice is case dependant.
- A choice of a small β, say 1e-6, can eliminate the dependence on the mass but can lead to instability of the network.
- As a rule of thumb, a log-linear dependence of the optimal β on the body radius could be considered. This radius is here considered to be R_0. Being the mass proportional to the cubic power of the body radius, then an (indirect) dependence on the mass is recovered.

In general, since it is possible to preliminary have information about the mass of the body that has to be visited (e.g. from inverse light curves or other methods), a tuning process of β is performed to recover the optimal β. Note that also in case this is not an option, the HNN could be robustly used to identify the mass of the body. This can be, then, used within the tuning process.

3.2. Dependency on body shape

In order to show the effect of the shape on β^*, the following analysis is performed:

- A tri-axial ellipsoid is defined by $(\alpha, 1, \gamma)$;

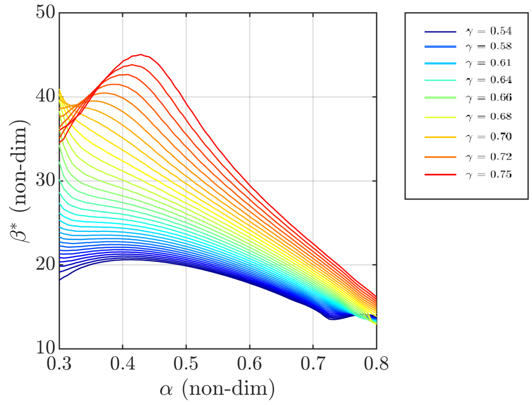

Figure 3: β^* dependency on (α, γ).

- a body with $R_0 = 1$km and an homogeneous density $\rho = 2200$ kg/m^3 is assumed;[6]
- $(3R_0, 0, 45°, 0, 0)$ is selected as orbital initial condition and the orbit is discretized in time with Δt of 30 seconds;
- the body's J_2 is estimated and the $iMSE$ is computed.

β^*, is extracted minimizing the $iMSE$. The results are presented in Fig. 3 where a slight dependence of β^* on the degree of body's irregularity is shown (here as irregularity is intended the non-roundness of the body). In particular, it can be seen that the more the body is regular the more the β^*s converge to a single value, while the more the irregular the body is, the more the β^* values are spread. This suggests that a fine tuning of the method could be beneficial in case of highly irregular bodies [16], however since the order of magnitude of β^* remains the same, the shape is considered an higher order parameter

[6] here R_0 is the Brillouin sphere.

of the problem, thus:

$$C_i(t_k) \approx s_i(\_,\_, a_0, e_0, i_0, \Omega_0, \omega_0, \beta, N_C, t_k, \mathbf{s}_0) \tag{29}$$

3.3. Dependency on the orbit

To highlight the dependency on the spacecraft orbit, the following analysis is performed:

- An oblate spheroid with flattening f=0.5 is defined, resulting in a tri-axial ellipsoid defined by $(1, 1, 0.5)$;
- a body with R_0 = 1km and ρ = 2200 kg/m^3 is assumed;
- the orbit is initialized as a function of a_0 and i_0: circular orbits are considered and the RAAN influence is not relevant since an oblate spheroid is considered.
- the orbital path discretized with Δt = 30 seconds and 10 revolutions about the body are considered.
- the body's J_2 is estimated and the $iMSE$ is computed.

The results for the $iMSE$ are presented in Fig. 4.

1. From Fig. 4a it seems that the dependence on the inclination of the orbit is *not* a dominant parameter. However, this is something not expected since zonal contributions to the potential is:

$$\mathcal{U}_{n,0} = -\frac{GM}{r}\left(\frac{R_0}{r}\right)^n J_n P_n(\cos\theta) \tag{30}$$

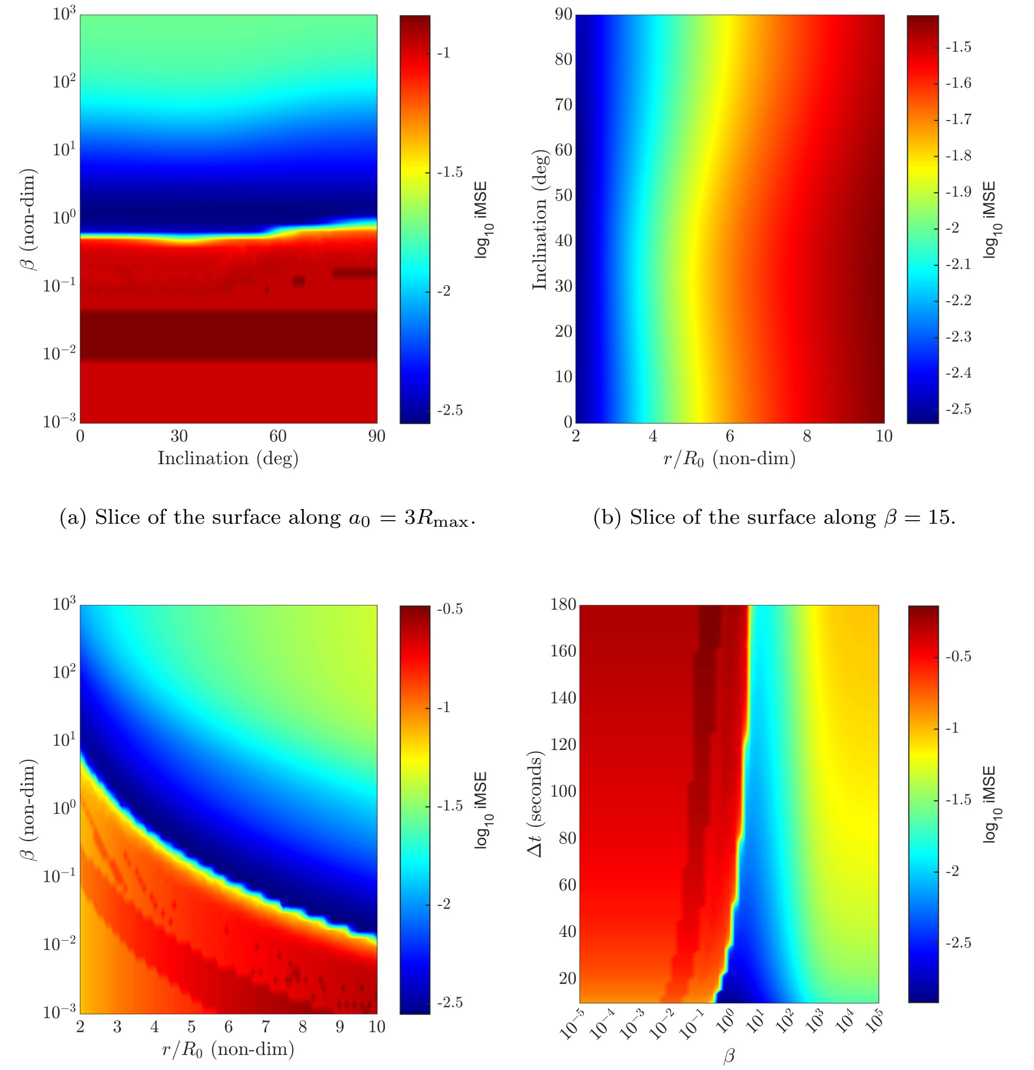

(a) Slice of the surface along $a_0 = 3R_{\max}$.

(b) Slice of the surface along $\beta = 15$.

(c) Slice of the surface along $i = 45$ °.

(d) Slice on $i = 45$ °, $r/R_0 = 3$.

Figure 4: Results for the orbit dependency test case. Different slices of the hyper-surface defined by Eq. 29 are presented.

i.e. it is experienced in case the colatitude $\theta \neq 0$. However, in this simplified case in which the only J_2 coefficient is estimated, the HNN is still capable to correctly

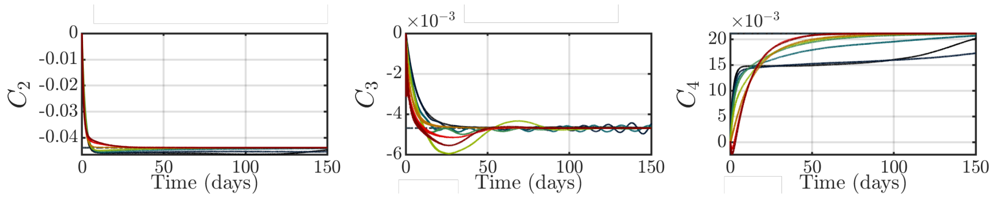

Figure 5: Network neural dynamics for $a_0 = 3R_0$, as a function of the orbit inclination (color scale - from black, $0°$ to red, $90°$)

estimate it. This is not the case for higher order harmonics, as can be seen from Fig. 5. Then, dependence on the orbit inclination is to be taken into account.

2. Fig. 4b shows instead that there is a stronger dependence on the distance to the body $r(t)$.
3. A cross-dependence between β and $r(t)$ is instead highlighted in Fig. 4c where it is evident that β^* has a decreasing monotonic behaviour with respect to $r(t)$. Note that on the top right of the surface the iMSE gets larger. This means that the network convergence velocity gets smaller (in all cases presented in this analysis the network do converge in the given time window).
4. Fig. 4d highlight a slight dependence on the time discretization Δt, coupled to the choice of β.

Thus, assuming to initialize the network with $\mathbf{s}_0 = \mathbf{0}$ (i.e. worst case, in which no prior information about the harmonics are available):

$$C_i(t_k) \approx s_i(r(t_k)/R_0, i_0, \beta, N_C, t_k, \mathbf{s}_0) = s_i(d(t_k), i_0, \beta, N_C) \tag{31}$$

Here $d(t_k) = r(t_k)/R_0$. Note that, as far as the orbit is non-equatorial, the depen-

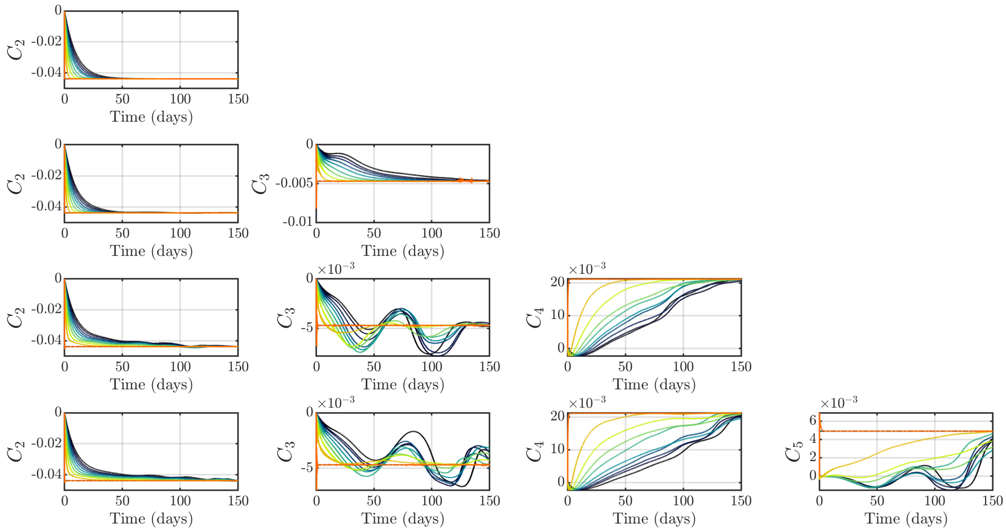

Figure 6: Neuron states dynamics as a function of the time, the number of the estimated coefficients and β (color scale, from black $\beta = 1$ to red $\beta = 10^{-6}$).

dency on the inclination can be considered to be an higher order one [16], thus:

$$C_i(t_k) \approx s_i(d(t_k), \beta, N_C) \tag{32}$$

3.4. Dependency on N_C

To highlight the dependency of the network state dynamics on the number of coefficients that are estimated a dedicated analysis is performed. In particular:

- An oblate spheroid with flattening f=0.5 is considered;
- a body with R_0 = 1km and ρ = 2200 kg/m^3 is assumed;
- the orbit is initialized with $a_0 = 2R_0$ and i_0=90°;

In Fig. 6 are presented the results: it can be noticed that there is a dependence on N_C, due to the cross correlated weights of the network, w_{ij}. However, this does not influence the ability of the network to correctly reconstruct the value of the coefficients, as far as a good choice of β is performed. Therefore, the neural state dynamics dependencies are reduced to:

$$C_i(t_k) = s_i(d(t_k), \beta^*) + \mathcal{O}(S, N_C) \tag{33}$$

3.5. Dependency on β

As a result of the previous discussion, the optimal tuning of the network hyperparameter β is function of:

- The body mass, M;
- The body degree of *irregularity*, S;
- The distance with respect to the body, $r(t)/R_0$;

i.e. Eq. 28 becomes:

$$\beta^* = \beta^*(M, S, d(t_k)) \tag{34}$$

Thus, there is no general rule for the optimal choice of β, however, according to [16] and [17] a reasonable initial guess to be used in a grid search can be extracted as a function of the body mass M as well as the orbit altitude $d(t_k)$. Then the initial guess can be refined for different body shapes with a grid search or multiple parallel executions of the network could be used in the estimation. Note that, according to [16], a choice of $\beta^* \approx 10^{-12}$ could in principle eliminate the dependence on the mass but such a small value would lead to network instability of higher order harmonics in real applications, especially for highly irregular bodies.

4. Applications to realistic gravitational environments

In this section a set of trajectories are generated considering the dynamical environments represented through the P2BP and the MCR3BP, in order to address the performances of the neural network in reconstructing the gravitational field of realistic objects in their gravitational environment. In order to simplify the approach to the problem, some assumptions are made:

1. The environment does not include SRP nor Sun third-body perturbation.
2. The orbital states are assumed to be reconstructed through a navigation filter. The state estimates are assumed to be the real ones perturbed with a zero-mean white Gaussian noise. In particular, position and velocity are perturbed by $\sigma_r = 10^2\ m$ and $\sigma_v = 10^{-2}\frac{m}{s}$, which are typical state's navigation uncertainties [28, 29].
3. Orbits with a retrograde acceleration component ($90° < i < 270°$) are preferred, for their inherent stability properties .
4. Orbit discretised with a time step of 30 seconds.

Moreover, since the parametric analysis shown an intrinsic dependency of the network convergence depending on the choice of the hyperparameter β, multiple networks are run together on the estimation of J_2, with different values of β for a given period of time and the *optimal* β^* is extracted. Then, the estimation is run again for all the coefficients to be identified, with the obtained β^* value.

To show the flexibility of the method, applications in different dynamical environments are presented. First of all, the HNN-based identification method is applied to some representative minor bodies, namely Castalia, Kleopatra and Phobos. Then, a binary system case is shown.

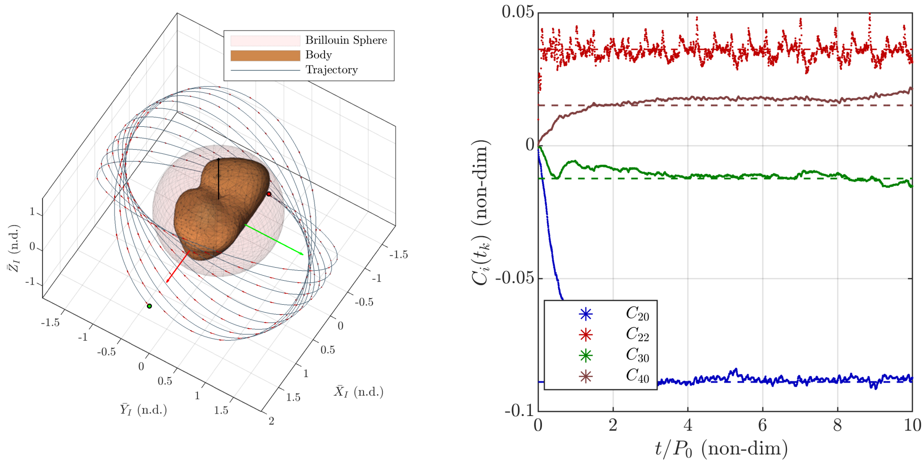

(a) Inertial body-centred frame orbit.

(b) HNN results.

Figure 7: Asteroid Castalia results: $a_0 = 2R_{max}$, $i_0 = 135°$ circular orbit. Dashed lines represent the true values of the coefficients.

4.1. Minor bodies representative cases: Castalia, Kleopatra and Phobos

In Figs. 7, 8, 9 are presented the results cases of Castalia, Kleopatra and Phobos, which are the minor bodies selected for this analysis. Here, the state vector is normalized using the maximum body radius R_{max} and the orbital time using the initial "Keplerian" orbital period P_0, in such a way the figures represent non-dimensional quantities. In Table 1 are presented the cumulative results for the identification of the Stokes coefficient of these bodies, which convergence is hereafter commented.

- **Castalia**: in this case, the optimal choice for β results to be 10^{-3} and the neuron dynamics is shown in Fig. 7b. Note that in this case the HNN is capable to reconstruct all the coefficients with a relatively small number of revolutions around the body.

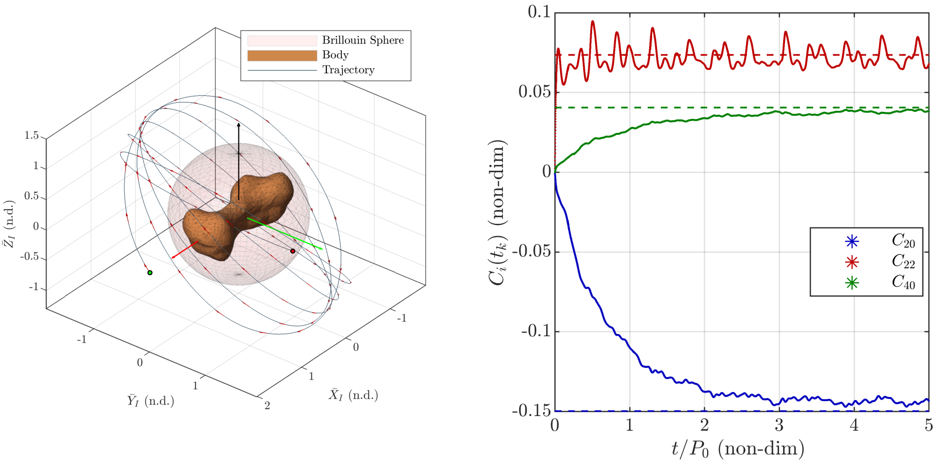

(a) Inertial body-centred frame orbit.

(b) HNN results.

Figure 8: Asteroid Kleopatra results: $a_0 = 2R_{max}$, $i_0 = 135°$ circular orbit. Dashed lines represent the true values of the coefficients.

- **Kleopatra**: also in this case, the optimal choice for β^* results to be 10^{-3}. However, to avoid network instabilities (see [16] for details of this phenomenon), a value of $1.5\beta^*$ is selected. As for the Castalia case, good convergence of all the coefficients is achieved.

- **Phobos**: in this case, due to the highly irregularity and the fast rotation of the body, a circular orbit is placed at higher altitude from the body surface, to avoid the possibility to crash on or escape from the body. Differently for the other cases, in this case the convergence exhibit *large* oscillations and an estimation offset. This can be due to the extremely chaotic environment generated by the fast-rotating body.

Note those results could be easily extended if other higher order gravitational pertur-

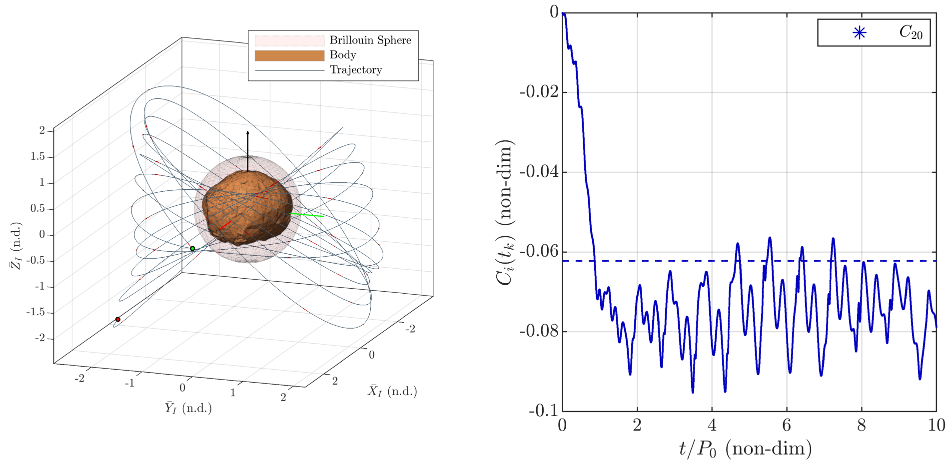

(a) Inertial body-centred frame orbit.

(b) HNN results.

Figure 9: Phobos case results: $a_0 = 3R_{max}$, $i_0 = 135°$ circular orbit. Dashed lines represent the true values of the coefficient.

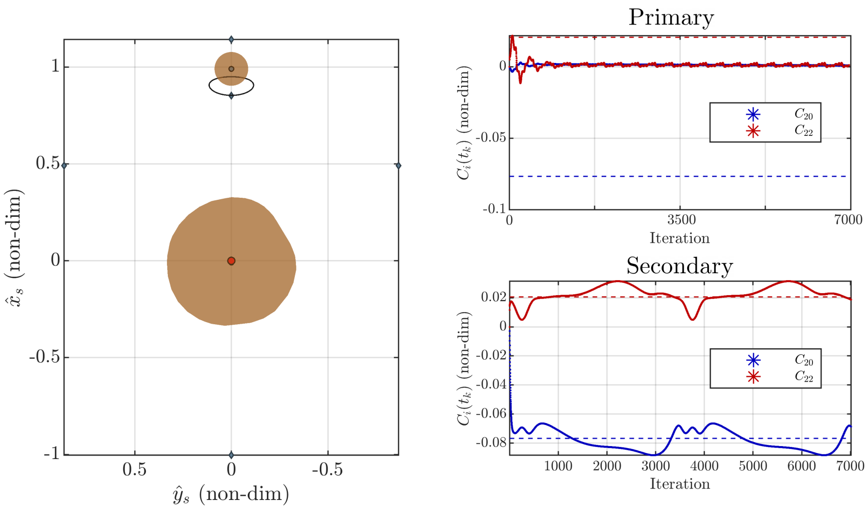

Figure 10: Didymos system, Southern Halo.

bations or non gravitational ones are taken into account. This can be seen in the example shown in Fig. 11, where the effect of the introduction of third-body perturbation (Sun) or SRP on the network neuron dynamics is presented. In particular, the third body

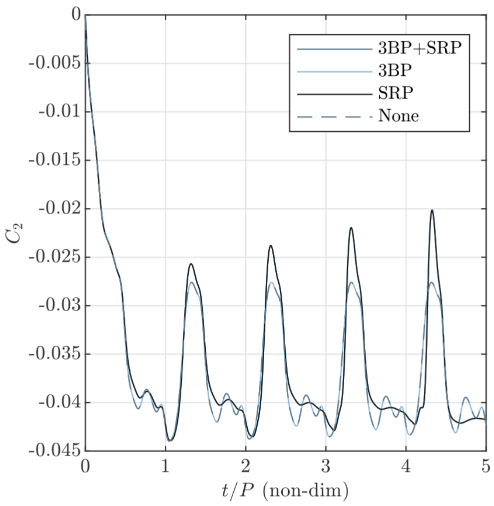

Figure 11: SRP and 3rd body perturbation effects on Castalia C_{20} convergence.

perturbation is shown to be negligible, while the SRP introduce a constant perturbation to the network (i.e. a linearly increasing term in time), which could be easily removed adding a simplified SRP model into the dynamical model used in the HNN.

4.2. Binary asteroids case: Didymos

The case of Didymos binary system is analysed in order to assess the scalability of the network to a different dynamical environment. According to [30], the dynamical environment can be represented through a polyhedron model for the primary body and a ellipsoid model for the secondary [31]. The network is implemented here in the un-normalized form associated to the SCR3BP. In this case, Ω_S as well as the mass of the two bodies is assumed to be known so that from Eq. 7:

$$\mathbf{y} = \ddot{\mathbf{r}} + \mathbf{\Omega}_S \times (\mathbf{\Omega}_S \times \mathbf{r}) + 2\mathbf{\Omega}_S \times \mathbf{r} + \frac{\mu_1}{r_1^3}\mathbf{r}_1 + \frac{\mu_2}{r_2^3}\mathbf{r}_2 \tag{35}$$

$$\mathrm{A} = [\mathrm{A}_{\mathrm{main}}(\mathbf{r}_1), \mathrm{A}_{\mathrm{moon}}(\mathbf{r}_2)] \tag{36}$$

Where the LIP form of Eq. 12 is $\mathbf{y} = \mathrm{A} \cdot \mathbf{C}_{\mathrm{ag}}$ where $\mathbf{C}_{\mathrm{ag}} = [\mathbf{C}_{\mathrm{main}}; \mathbf{C}_{\mathrm{moon}}]$. Some orbital families were analysed in order to assess the capability of the network to work in such a perturbed environment.

In this paper, the results for the case of a L1 Halo orbit are presented in Fig. 10. This trajectory is chosen for the presence of out-of-plane components, fundamentals in the identification of zonal harmonics, as well as, being in L1, give the possibility to test the network sensitivity to both the primary and the secondary gravity harmonics. In this case an optimal β value is selected to be 10^{-7}, to boost the sensitivity of the network. However, it can be seen that, while the Dimorphos harmonics are well reconstructed (in mean), the method is not capable to properly capture Didymos harmonics. This is apparently in contrast with radio science simulations [32], but is due to the network tuning, which in this case was optimised for Dimorphos' harmonics reconstruction.

5. Comparison with EKF-based Parameter Identification

The parameter identification problem has been studied in different technical disciplines. One common technique to estimate internal parameters of nonlinear systems is to use an augmentation of the traditional Extended Kalman Filter, under certain observability conditions [33]. The comparison presented hereby focuses on evaluating two approaches both relying on Extended Kaman Filter techniques, in particular:

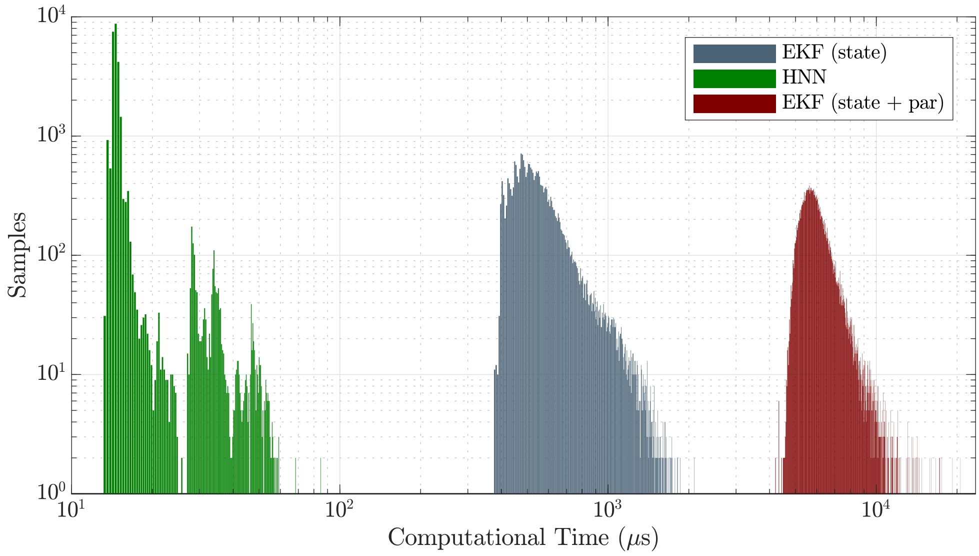

Figure 12: Computational time comparison. Note that the HNN step-time is negligible with respect to the EKF for state estimation.

1. **Coupled EKF-HNN**: the EKF is coupled with the presented HNN. The filter is dedicated to reconstruct the state vector of the system, whereas the HNN approximates the unknown spherical harmonics coefficients. The coupling between the EKF and HNN could be performed by using the reconstructed HNN coefficients in the prediction step of the EKF, i.e. adopting the Spherical Harmonics Expansion as gravitational model in the filter process model. Nevertheless, for coefficient reconstruction purposes, the performance results to be equivalent if the point-mass gravity is adopted instead of the SHE, as shown in Fig. 13. In particular, the figure presents the difference in the convergence in the case in which the network receive the state vector from the true dynamics propagation (red), the EKF estimation with a point mass gravity model (blue) and the EKF estimation with SHE model (coupled case, grey). It can be noticed that not major differences are present in

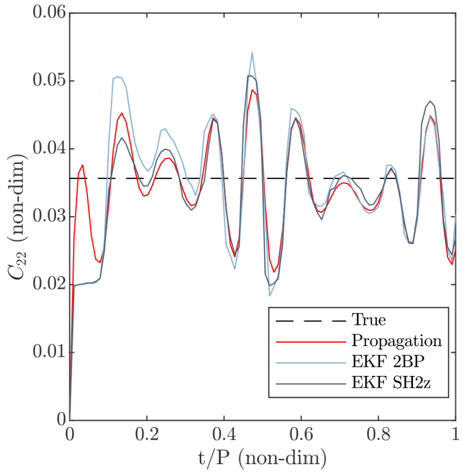

Figure 13: HNN convergence comparison of the effect of different input sources to the network.

case the point-mass of the SHE model are considered within the EKF.

2. **Augumented EKF**: the EKF is used both for estimating the state and the unknown coefficients. Thus, the augmented state of the filter comprises the set of coefficients to be identified.

In order to compare the performance of the HNN approach for estimating spherical harmonics coefficients, an EKF-based estimation algorithm has been developed as in [34] for both cases and are specified in the following sections.

5.1. Augmented filter formulation

In this section the augmented filter formulation is presented. In particular, the state vector of the EKF is augmented as follows:

$$\mathbf{X} = \begin{bmatrix} \mathbf{r} \\ \mathbf{v} \\ C_{nm} \end{bmatrix} \tag{37}$$

where $\mathbf{r}$ and $\mathbf{v}$ are the position and velocity vectors respectively; $\{C_{nm}\}$ is a stacked vector containing the SHE coefficient, whose length depends on the application scenario being N_C the number of coefficient. The dynamics of the augmented state space resembles the one presented for the HNN-based algorithm, namely:

$$\dot{\mathbf{X}} = \begin{bmatrix} \mathbf{v} \\ \nabla\mathcal{U}\left(\mathbf{r}, C_{nm}\right) + 2\boldsymbol{\Omega} \times \dot{\boldsymbol{r}} + \boldsymbol{\Omega} \times (\boldsymbol{\Omega} \times \mathbf{r}) \\ 0_{nm} \end{bmatrix} \tag{38}$$

where it is important to note that the gradient of the potential is dependent on the estimated SHE coefficients. This guarantees system observability for estimating the aforementioned internal parameters. The state transition matrix is approximated using the first order Taylor expansion [28], so that the Jacobian of the dynamics, which is calculated analytically, can be constructed as follows:

$$\mathbf{J} = \begin{bmatrix} \mathbf{0}_{3\times3} & \mathbf{I}_{3\times3} & \mathbf{0}_{3\times p} \\ \nabla^2\mathcal{U} & \mathcal{M}_\Omega & \mathrm{A}(\mathbf{r}) \\ \mathbf{0}_{p\times3} & \mathbf{0}_{p\times3} & \mathbf{0}_{p\times p} \end{bmatrix} \tag{39}$$

where $\mathcal{M}_\Omega = \frac{\partial\nabla\mathcal{U}}{\partial\mathbf{v}} = 2[\boldsymbol{\Omega}\times]$.

For the sake of simplicity, in this paper the EKF measurement equation is assumed to be linear, with the measurement matrix reading:

$$\mathbf{H} = [\mathbf{I}_{6\times6}\ \mathbf{0}_{nm}] \tag{40}$$

Therefore the complete algorithm, including the update step, is reported in Algorithm 1.

Algorithm 1 EKF

$\hat{\mathbf{X}}_k^- = \int_{t_{k-1}}^{t_k} f(\mathbf{X}(\tau))d\tau, \quad \mathbf{X}_{k-1} = \hat{\mathbf{X}}_{k-1}, \quad \hat{\mathbf{X}}_0^+ = \mathbf{X}_0$

$\mathbf{J}_k = \left.\frac{\partial f}{\partial \mathbf{X}}\right|_{\hat{\mathbf{X}}_{\mathbf{k-1}}}, \mathbf{H}_k = \mathbf{H}$

$\mathbf{P}_k^- = \mathbf{\Phi}(t_k, t_{k-1})\mathbf{P}_{k-1}^+\mathbf{\Phi}^T(t_k, t_{k-1}) + \mathbf{Q}, \quad \mathbf{P}_0^+ = \mathbf{P}_0$

$\mathbf{K}_k = \mathbf{P}_k^-\mathbf{H}_k^T(\mathbf{H}_k\mathbf{P}_k^-\mathbf{H}_k^T + \mathbf{R}_k)^{-1}$

$\hat{\mathbf{X}}_k^+ = \hat{\mathbf{X}}_k^- + \mathbf{K}_k(\mathbf{Y}_k - \mathbf{H}\mathbf{X}_k^-)$

$\mathbf{P}_k^+ = (\mathbf{I} - \mathbf{K}_k\mathbf{H}_k)\mathbf{P}_k^-(\mathbf{I} - \mathbf{K}_k\mathbf{H}_k)^T + \mathbf{K}_k\mathbf{R}\mathbf{K}_k^T$

Here the process covariance matrix $\mathbf{Q}$ is assumed to be fixed in time and after a brute force tuning process, is considered to be equal to:

$$\mathbf{Q} = \mathrm{diag}(\left[s_r^2 \cdot \texttt{ones}(3),\, s_v^2 \cdot \texttt{ones}(3),\, s_C^2 \cdot \texttt{ones}(N_p)\right]) \tag{41}$$

where N_p is the number of coefficients to be estimated, $\texttt{ones}(x)$ is an operator that provide a vector of ones of length x, s_r = 1e-1, s_v = 1e-3 and $s_C = 0$. Real application scenarios of an asteroid mission will require more sophisticated measurement function and behavioural model relying on low-observability measurements, as described in [28].

5.2. Numerical results and comparison

The dynamical environment described in Section 2.1 is used for numerical simulations. The measurements are generated through propagation of the aforementioned dynamical models. Furthermore, the state measurements are assumed to be perturbed with zero-mean white Gaussian noise. In particular, position and velocity are perturbed using $\sigma_r = 10^2\ m$ and $\sigma_v = 10^{-2}\,\frac{m}{s}$. For the sake of comparison, three test cases have been assessed, namely asteroids Castalia, Kleopatra and the moon Phobos.

For the parametric identification of gravitational field coefficients, being the number

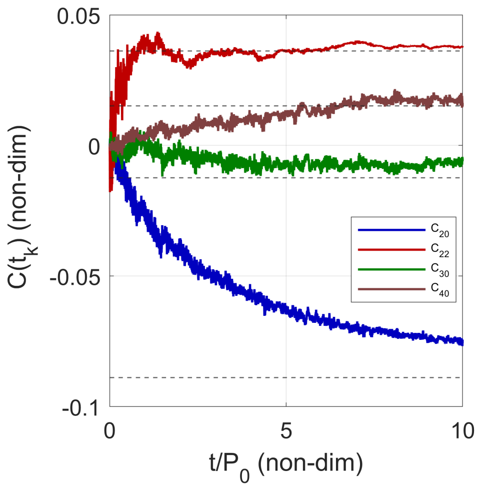

(a) Castalia

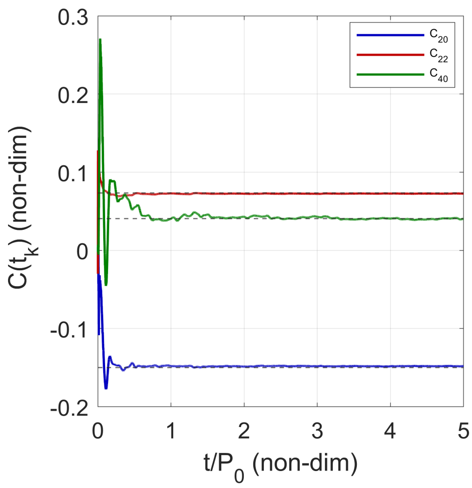

(b) Case Kleopatra

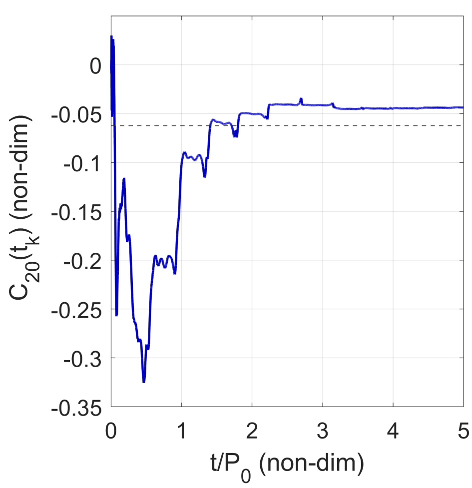

(c) Phobos

Figure 14: SHE coefficients estimation using EKF.

of parameters always >1 and usually $\gg 1$, the use of a method other than the EKF can be beneficial from a computational point of view. In fact the computational cost of a filter step do increase at least linearly with the number of elements of the augmented vector $\mathbf{X}$. In Fig. 12 a comparison between the two methods is presented considering the case of asteroid Castalia (4 parameters):

- In green, the computational time for a single step of the HNN is reported. The mean $\mu_{\mathrm{hnn}} \sim 15$ μs while the standard deviation $\sigma_{\mathrm{hnn}} \sim 12$ μs.
- In grey, the computational time for a single step of a EKF used for the state-only estimation is reported. In this case, the mean $\mu_{\mathrm{hnn}} \sim 600$ μs while the standard deviation $\sigma_{\mathrm{hnn}} \sim 386$ μs. The gravitational model used in the EKF in this case is the pure Two-Body Problem.
- In red, the computational time for a single step of a EKF used for both the state and the parameters estimation. In this case, the mean $\mu_{\mathrm{hnn}} \sim 6.25$ ms while the standard deviation $\sigma_{\mathrm{hnn}} \sim 2.15$ ms.

The previous results are computed on a machine with a quad-core, i7-7700, 3 GHz CPU and highlight that the computational time associated to a EKF+HNN in the state & parameters estimation is one order of magnitude smaller than the one associated to an augmented EKF, being beneficial also from a volatile memory point of view.

From the parameters estimation point of view, instead, both the methods are capable to reconstruct the selected Stokes coefficients, as reported in Tab. 1. In particular, for asteroid Castalia, the HNN estimation results are presented in Fig. 7 while the one associated to the EKF in Fig. 14a: in this case the HNN exhibit better convergence properties with respect to the filter that converges slower. It is the opposite for the case of asteroid Kleopatra, Fig. 8, Fig. 14b. Finally, in the case of Phobos, that is critical for the highly perturbed environment associated to the large centrifugal forces, both methods have troubles in the estimation, giving an offset on the final estimate. Note that, in general, the coefficients estimated by the EKF results to be more *stable* than the one computed by the HNN. This issue can be easily solved choosing a more conservative value for β and allowing the network to run longer in time.

As a drawback, the HNN is not capable to quantify the uncertainty of the reconstructed coefficients. However, the temporal evolution of the reconstructed term may be used to derive the variance of the signal and therefore recover an indication on the uncertainty. Moreover, running more than one HNN in parallel, could be used as an unscented approach to estimate coefficients uncertainty.

6. Conclusions

In this paper, the exploitation of an HNN for spherical harmonics coefficients identification and the comparison between EKF and an HNN for the parameter estimation of the gravitational field of small bodies were analysed. The criticalities of the HNN for this task have been highlighted and consist in the tuning of the activation function through a parameter β. This parameter β results to be dependant on the distance to the body mainly and to have a dependence on the degree of irregularity of the visited body. In particular, for high irregular cases, a conservative choice of β should be made. These results are then validated in the real gravitational environment of some selected bodies, namely Castalia, Kleopatra and Phobos. The case of a binary system (Didymos) is presented too: the re-formulation of the network' associated dynamics appears to be simple as well as all the consideration valid for a single body can be used for the tuning of the network. From the other hand, the same tests are performed with an augmented-EKF. The performance of the EKF, as expected, results to be good also in this task. However,

Table 1: HNN/EKF results compared for Castalia, Kleopatra and Phobos. The root mean square error and the standard deviation are computed on the last 5 periods of a 10 periods simulation.

	True	HNN (RMSe)	HNN (std)	EKF (RMSe)	EKF (std)
			Castalia		
C_{20}	-0,089	2,0e-3	6,5e-4	1,93e-2	3,5e-3
C_{22}	0,0362	7,0e-4	2.78e-3	8,0e-4	1,2e-3
C_{30}	-0,0124	2,6e-3	7.35e-4	7,0e-3	1,3e-3
C_{40}	0,0152	1,64e-3	5.46e-4	3,7e-3	1,2e-3
			Kleopatra		
C_{20}	-0,149	1,1e-2	1,77e-3	0,0	1e-7
C_{22}	0,0734	4,6e-3	4,52e-3	0,0	1e-7
C_{40}	0,0405	7,0e-4	2,42e-4	0,0	4e-7
			Phobos		
C_{20}	-0,0622	1,6e-2	2,67e-2	1,3e-2	4,8e-4

from the computational point of view, the augmented-EKF result to be heavier than the couple EKF+HNN. Finally, from the previous results we can conclude that the use of a HNN online gravity field estimation is a good alternative to an EKF as well as can be use to validate the results of the filter itself.

Future works include application of the presented methodology to autonomous guidance algorithms.

References

[1] J. Miller, A. Konopliv, P. Antreasian, J. Bordi, S. Chesley, C. Helfrich, W. Owen, T. Wang, B. Williams, D. Yeomans, D. Scheeres, Determination of shape, gravity, and rotational state of asteroid 433 eros, Icarus 155 (2002). doi:10.1006/icar.2001.6753.

[2] A. Konopliv, S. Asmar, R. Park, B. Bills, F. Centinello, A. Chamberlin, A. Ermakov, R. Gaskell, N. Rambaux, C. Raymond, et al., The vesta gravity field, spin pole and rotation period, landmark positions, and ephemeris from the dawn tracking and optical data, Icarus 240 (2014) 103–117.

[3] M. Pätzold, T. Andert, M. Hahn, S. Asmar, J.-P. Barriot, M. Bird, B. Häusler, K. Peter, S. Tellmann, E. Grün, et al., A homogeneous nucleus for comet 67p/churyumov–gerasimenko from its gravity field, Nature 530 (7588) (2016) 63–65.

[4] V. Pesce, S. Silvestrini, M. Lavagna, Radial basis function neural network aided adaptive extended Kalman filter for spacecraft relative navigation, Aerospace Science and Technology 96 (2020) 105527. doi:10.1016/j.ast.2019.105527.

[5] S. Silvestrini, M. Lavagna, Neural-aided GNC reconfiguration algorithm for distributed space system: development and PIL test, Advances in Space Research 67 (5) (2021) 1490–1505. doi:10.1016/j.asr.2020.12.014.

[6] S. Silvestrini, M. Lavagna, Neural-Based Predictive Control for Safe Autonomous Spacecraft Relative Maneuvers, Journal of Guidance, Control, and Dynamics (2021). doi:10.2514/1.G005481.

[7] R. Furfaro, R. Linares, V. Reddy, J. Simo, L. Le Corre, Modelling irregular small bodies gravity field via extreme learning machines, in: 27th AAS/AIAA Spaceflight Mechanics Meeting, 2017.

[8] S. Willis, D. Izzo, D. Hennes, Reinforcement learning for spacecraft maneuvering near small bodies, in: AAS/AIAA Space Flight Mechanics Meeting, 2016, pp. 14–18.

[9] A. Gao, W. Liao, Efficient gravity field modeling method for small bodies based on gaussian process regression, Acta Astronautica 157 (2019) 73–91.

[10] B. Turgut, Application of back propagation artificial neural networks for gravity field modelling, Acta Montanistica Slovaca 21 (2016) 200–207.

[11] A. Gret, E. Klingele, H.-G. Kahle, Application of artificial neural networks for gravity interpretation in two dimensions: a test study, Bollettino di Geofisica Teorica ed Applicata 41 (2000) 1–20.

[12] Y. Wu, H. Wang, B. Zhang, K.-L. Du, Using radial basis function networks for function approximation and classification, ISRN Applied Mathematics 2012 (03 2012). `doi:10.5402/2012/324194`.

[13] M. Reza Jafari, T. Alziadeh, G. Mehdi, A. Alizadeh, K. Salahshoor, On-line identification of nonlinear systems using an adaptive rbf-based neural network, Lecture Notes in Engineering and Computer Science 2167 (10 2007).

[14] N. Harl, K. Rajagopal, S. N. Balakrishnan, Neural network based modified state observer for orbit uncertainty estimation, Journal of Guidance, Control, and Dynamics 36 (4) (2013) 1194–1209. `arXiv:https://doi.org/10.2514/1.55711`, `doi:10.2514/1.55711`.
URL `https://doi.org/10.2514/1.55711`

[15] D. Scheeres, Orbital mechanics about small bodies, Acta Astronautica 72 (2012) 1–14.

[16] A. Pasquale, Small bodies gravity field on-board learning and navigation, Master's thesis, Politecnico di Milano, Milan (2019).

[17] A. Pasquale, S. Silvestrini, A. Capannolo, M. Lavagna, Non-uniform gravity field model on board learning during small bodies proximity operations, in: International Astronautical Congress, 2019.

[18] R. A. Werner, Spherical harmonic coefficients for the potential of a constant-density polyhedron, Computers & Geosciences 23 (10) (1997) 1071 – 1077. `doi:https://doi.org/10.1016/S0098-3004(97)00110-6`.
URL `http://www.sciencedirect.com/science/article/pii/S0098300497001106`

[19] W. MacMillan, The Theory of Potential, Dover Publications, 1958.

[20] D. Scheeres, Orbital motion in strongly perturbed environments: application to asteroid comet and planeraty satellite orbiters, Springer, 2012.

[21] Y. Takahashi, Gravity field characterization around small bodies, Ph.D. thesis, University of Col-

orado Boulder (2013).

[22] H. Alonso, T. Mendonça, P. Rocha, Hopfield neural networks for on-line parameter estimation, Neural networks : the official journal of the International Neural Network Society 22 (2009) 450–62.

[23] M. Atencia, G. Joya, F. Sandoval, Parametric identification of robotic systems with stable time-varying hopfield networks, Neural Computing and Applications 13 (2004) 270–280.

[24] J. J. Hopfield, Neurons with graded response have collective computational properties like those of two-state neurons, Proceedings of the National Academy of Sciences 81 (10) (1984) 3088–3092.

[25] Abe, Theories on the hopfield neural networks, in: International 1989 Joint Conference on Neural Networks, 1989, pp. 557–564 vol.1.

[26] M. Atencia, G. Joya, F. Sandoval, Hopfield neural networks for parametric identification of dynamical systems, Neural Processing Letters 21 (2005) 143–152.

[27] Y. Hernández-Solano, M. Atencia, G. Joya, F. Sandoval, A discrete gradient method to enhance the numerical behaviour of hopfield networks, Neurocomput. 164 (C) (2015) 45–55.

[28] S. Silvestrini, A. Capannolo, M. Piccinin, M. Lavagna, J. Gil-Fernandez, Centralized Autonomous Relative Navigation of Multiple Spacecraft Around Small Bodies, in: AIAA Scitech 2020 Forum, no. January, 2020, pp. 1–20. doi:10.2514/6.2020-1204.

[29] S. Silvestrini, A. Capannolo, M. Piccinin, M. Lavagna, J. G. Fernandez, Centralized autonomous relative navigation of multiple spacecraft around small bodies, The Journal of the Astronautical Sciences 1 PartF (2020). doi:10.2514/6.2020-1204.

[30] L. Dell'Elce, N. Baresi, S. Naidu, L. Benner, D. Scheeres, Numerical investigation of the dynamical environment of 65803 didymos, Advances in Space Research (2017).

[31] A. Capannolo, F. Ferrari, M. Lavagna, Families of bounded orbits near binary asteroid 65803 didymos, Journal of Guidance, Control, and Dynamics 42 (1) (2019) 189–198.

[32] M. Zannoni, I. Gai, M. Lombardo, E. Gramigna, R. Lasagni Manghi, P. Tortora, O. Karatekin, H. Goldberg, P. Martino, M. Kueppers, et al., Didymos gravity science investigations with the hera mission, in: European Planetary Science Congress, 2020, pp. EPSC2020–691.

[33] R. Munguía, S. Urzua, A. Grau, EKF-based parameter identification of multi-rotor unmanned aerial vehiclesmodels, Sensors 19 (19) (2019) 1–17.

[34] Z. Xu, N. Qi, Y. Chen, Parameter estimation of a three-axis spacecraft simulator using recursive least-squares approach with tracking differentiator and extended kalman filter, Acta Astronautica

117 (2015) 254–262.